ELSEVIER

Journal of Fluids and Structures 24 (2008) 75–95

JOURNAL OF FLUIDS AND STRUCTURES

www.elsevier.com/locate/jfs

Computing the aeroelastic disk vibrations in a hard disk drive

S. Kirpekar[a,*], D.B. Bogy[b]

[a]*Hitachi Global Storage Technologies, 5600 Cottle Road, San Jose, CA 95193, USA*
[b]*Computer Mechanics Laboratory, Department of Mechanical Engineering, University of California at Berkeley, Berkeley, CA 94720, USA*

Received 5 July 2006; accepted 6 July 2007
Available online 1 November 2007

Abstract

The turbulent flow of air caused by the spinning of a single disk inside a typical hard disk drive casing is calculated using large eddy simulation (LES). The pressure acting on the disk is recorded as a function of time and is used to compute the vibrations of the spinning disk using a self-developed hybrid-spectral finite-difference code. This unidirectional fluid–structure interaction problem is computed for two commonly occurring cases: a disk actuated on one side only (Case 1) and a disk actuated on both sides (Case 2). The pressure loading on the disk is characterized in terms of its mean, root-mean-square (r.m.s.) and its spectral content. The mean pressure acting on the disk is asymmetrical in the case where the disk is actuated on one side only, leading to a mean deformation of the disk to one side. The r.m.s. vibrations of Case 2 are higher than those for Case 1 and their spectral distributions are almost identical. Large pressure fluctuations of the flow are found in the wake of the actuator arm and near the region where the shroud expands to accomodate the actuator. The spectral content of the excitation force due to the pressure is mainly in the low kHz frequency range, while higher frequencies are seen at the disk edge. This typically results in the excitation of the first 3–4 modes of the disk; however, (asymmetric) Case 1 displays the excitation of higher modes compared with (symmetric) Case 2.

Keywords: Hard disk drives; Airflow; Large eddy simulation; Disk vibration; Disk flutter

1. Introduction

The rotating disk is the principal mechanical component of a hard disk drive. The dynamic stability of the disk in its transverse motion is of great importance to the successful operation of the hard drive. Over the years, the need for faster data transfer rates has led to an increase in rotational speeds of disk drives. However, the dynamic stability of the disk itself is not the only concern. Read–write heads in modern hard disk drives are positioned only a few nanometers adjacent to these rotating disks by means of air-bearing sliders. Due to the nonlinear coupled nature of the head–disk interface transverse vibrations of the disk may cause significant sideways motions (“off-track” motions) of the slider-head. Such off-track motions are detrimental to the accurate positioning of the read–write head on data tracks. In more extreme situations disk vibrations may lead to the slider crashing on the disk, which results from a breakdown of the air bearing, possibly damaging the disk and/or the slider and contaminating the drive with wear particles.

*Corresponding author.
E-mail address: Sujit.Kirpekar@hitachigst.com (S. Kirpekar).

0889-9746/$ - see front matter © 2007 Elsevier Ltd. All rights reserved.
doi:10.1016/j.jfluidstructs.2007.07.005

Increasing spindle motor speeds have also led to the possibility of disks achieving their critical speed, which is the minimum rotational speed at which the backward traveling waves become standing waves on the disk. Due to the stationary forcing of the air-bearing slider, such standing waves quickly become resonant, leading to high amplitude vibrations of the disk. Experimental data shows that current disk drives operate at approximately 40–50% of their critical speeds but increasing drive rpms and the need for thinner disks may bring such disks closer to the critical resonance. Disks which operate in the super-critical speed regime (e.g. floppy disks which are designed to do so) have the additional risk of undergoing hydrodynamically coupled resonant vibrations called "flutter". While this is not a concern for thicker and stiffer hard disks, the airflow results that we present may also be used as a model to simulate the aeroelastic vibrations of floppy disks.

1.1. Prior work

The vibrations and stability of a spinning disk have been studied for almost a century now. There have been significant advances both in the fluid mechanics of flows surrounding spinning disks and the structural vibrations induced by such flows. A number of authors have studied the aeroelastic stability (stability to self-excited vibrations) of spinning disks. For a summary of this research, see references [1]–[12] in Kang and Raman (2004). Some investigations have used unenclosed rotating disks while others have used more realistic enclosed rotating disks. Most of the efforts, however, have used either ad hoc rotating damping operators to model the surrounding flow or hydrodynamic lubrication theory to model the coupling of the flow with the disk. Generally, such models based on compressible potential flow are suitable for floppy disks or circular saws, where the air film thickness is small. In hard disk drives, in addition to a large air film thickness (2–3 times the thickness of the disk), the azimuthal symmetry of the flow is broken by the presence of the actuator. This obstruction causes rapid unsteady motions in the wake of its sheds. The turbulent wake is transported (and dissipated) with the rotating disks and comes around to flow over the obstruction again. It is unlikely for such a complicated turbulent flow to be ever described by an analytical model. Moreover, given the complicated and frequently changing design of actuator components (such as the suspension), the only feasible method to compute realistic disk vibrations would be to solve for the flow in a separate CFD calculation and use the pressure and shear data to compute the disk vibrations.

For commercially available hard drives, experimental results suggest (Fukaya et al., 2002) that the vibrations of the disk are independent of the instability of the flow. Moreover in typical hard disk drives, the experimentally measured vibrations of disks (due to all sources) are less than 0.1% of the width of the entire hard drive enclosure and the maximum linear speed of disks is approximately 10% of the acoustic speed in air. All this implies that compressible effects of the flow may be small, while the turbulence-induced effects on the disk vibration may be larger.

In general accurate information about disk vibrations computed using CFD-based air pressure data is lacking.

Tatewaki et al. (2001) provide LES results from a coupled CFD-structural calculation in which they report the vibrations of the disk with and without a simplified obstruction. Yuan et al. (2004) computed the flow in a deformed disk enclosed inside a casing but with an open shroud. They present results for the pressure and shear forces on the disk in its deformed umbrella-like shape as a function of the Reynolds number. Unfortunately their model did not have any obstruction (e.g. an actuator) and hence resulted in a completely different flow field from what is encountered in a disk drive. Also the deflection of the disk was unreasonably large: 25% of the width of the entire hard drive enclosure, while it is typically of the order of 0.1%.

Imai (2001), Chang et al. (2002) and Guo and Chen (2001), provide experimental measurements of disk vibrations. These are then converted to off-track slider motions using the mode shapes of the disk and are correlated with the position error signal.

1.2. Motivation

The specific goals of this work are as follows:

(i) To study the flow on both sides of a single spinning disk in a fixed hard drive casing, using large eddy simulation (LES);
(ii) To characterize the pressure loading on the disk and bring out the essential physical processes that take place in such flows;
(iii) To develop an efficient and accurate solver to compute the free or forced vibrations of a spinning disk and to test the solver comprehensively;
(iv) To use the solver to compute the response of the disk to realistic loadings thus providing the disk drive community more realistic simulation results of the flow-induced disk vibrations.

2. Theoretical background

The equations of transverse motion of a spinning disk are well known since Lamb and Southwell (1921). The governing equations may be extended to include the forcing due to the airflow excitation and the air-bearing force due to the slider. These equations are given by

$$\rho h(w_{,tt}+2\Omega w_{,t\phi}+\Omega^2 w_{,\phi\phi})+\frac{Eh^3}{12(1-v^2)}\nabla^4 w-\frac{h}{r}(\sigma_{rr}rw_{,r})_{,r}-\frac{h\sigma_{\phi\phi}}{r^2}w_{,\phi\phi}=\Delta p+\frac{1}{r}\delta(r-\xi)\delta(\phi)f_z, \tag{1}$$

where w is the transverse displacement of a point on the disk, ρ is the density of the disk material, h is the thickness of the disk, Ω is the speed of rotation of the disk, and E and v are the Young's modulus and Poisson's ratio of the disk material. The slider is modeled to exert a force f_z (which is the gram load of the slider, chosen here as 2 g) at a radius of ξ at $\phi=0$ using the Dirac delta function $\delta(:)$. The unsteady distributed loading on the disk due to the airflow is given by $\Delta p=\Delta p(r,\phi,t)=p_{\text{bottom}}-p_{\text{top}}$. In polar coordinates, the biharmonic operator is given by

$$\nabla^4=\left(\frac{\partial^2}{\partial r^2}+\frac{1}{r}\frac{\partial}{\partial r}+\frac{1}{r^2}\frac{\partial^2}{\partial\phi^2}\right)^2. \tag{2}$$

Eq. (1) assumes that the material of the disk is homogeneous, isotropic and linearly elastic (Hookean). The transverse displacements of the disk are assumed to be much smaller than its thickness ($w\ll h$) and the stress state of the disk is assumed to be one of generalized plane stress. Ω is also assumed to be constant. For a derivation of the full nonlinear equations of motion the reader is referred to Chung et al. (2000). The self-adjoint stiffness operator

$$\mathbb{K}[w]=\frac{Eh^3}{12(1-v^2)}\nabla^4 w-\frac{h}{r}(\sigma_{rr}rw_{,r})_{,r}-\frac{h\sigma_{\phi\phi}}{r^2}w_{,\phi\phi} \tag{3}$$

models the bending stiffness as well as the stiffness caused by the membrane stress tensor σ. The diagonal terms of the membrane stress tensor are σ_{rr} and $\sigma_{\phi\phi}$, while the off-diagonal term $\sigma_{r\phi}$ is assumed to be zero, by which we are assuming that the membrane stress in axisymmetric. The generalized plane stress expressions for the stress components σ_{rr} and $\sigma_{\phi\phi}$ are

$$\sigma_{rr}=c_1+\frac{c_2}{r^2}-\frac{3+v}{8}r^2\Omega^2,\quad \sigma_{\phi\phi}=c_1-\frac{c_2}{r^2}-\frac{1+3v}{8}r^2\Omega^2; \tag{4,5}$$

the constants c_1 and c_2 may be determined by the application of boundary conditions. The most commonly used model is to require that the inplane displacement goes to zero at the inner clamp and the stresses go to zero at the free outer rim of the disk. [For some other models we refer the reader to the thesis of D'Angelo (1991).] Finally, the constants may be evaluated as

$$c_1=\Omega^2\left(\frac{1+v}{8}\rho\frac{(v-1)r_o^4-(3+v)r_i^4}{(v-1)r_o^2-(1+v)r_i^2}\right),\quad c_2=\Omega^2\left(\frac{1-v}{8}\rho r_i^2r_o^2\frac{(1+v)r_o^2-(3+v)r_i^2}{(v-1)r_o^2-(1+v)r_i^2}\right), \tag{6,7}$$

where r_i and r_o denote the inner and outer radii of the disk.

There are four radial boundary conditions associated with Eq. (1). At $r=r_i$ the transverse displacement and its rotation (slope) are zero,

$$w=0,\quad \frac{\partial w}{\partial r}=0; \tag{8}$$

and at $r=r_o$ the radial bending moment and the shear force reaction are zero:

$$w_{,rr}+v\left(\frac{1}{r}w_{,r}+\frac{1}{r^2}w_{,\phi\phi}\right)=0,\quad (\nabla^2 w)_{,r}+(1-v)\frac{1}{r}\left[\left(\frac{1}{r}w_{,\phi}\right)_{,r}\right]_{,\phi}=0. \tag{9}$$

Note that Eq. (1) does not include any damping terms. Material damping of aluminum substrates used in hard disks is known to be significant (Kim et al., 2000). Hosaka and Crandall (1992) modeled this material damping as a term proportional to $\nabla^4 w_{,t}$. The other sources of damping are due to the clamping of the disk at its inner radius and the shear stress due to the drag of the flow on the disk surface. In our simulations each source of dissipation was not treated separately, but a global dissipation matrix was constructed from a linear combination of the mass and stiffness matrices (commonly referred to as proportional damping or Rayleigh damping). In supercritical vibrations of flexible disks, certain types of damping (e.g. acoustic damping and material damping) are known to cause the onset of flutter instabilities in which case different sources of damping need to be modeled carefully (Kang and Raman, 2004).

However, for our lower speed subcritical disks, a single proportional damping operator does suffice. The amount of dissipation for a range of frequencies was selected based on the aeroelastic parameters given in the experimental data of Kim et al. (2000). Typically, the first mode of the disk is damped at about 0.02% of critical damping.

3. Numerical methods

Our calculations were broadly divided into two parts. In the first part we calculated the flow of air in a simulated hard disk enclosure using a commercial CFD software and recorded the pressure data on the two sides of the disk as a function of time. In the next part of the calculation we used this time-varying pressure data to compute the vibrations of the disk using a software program developed by us. The vibrations of the disk were not fed back into the CFD solver; thus the coupling was purely unidirectional, i.e. from the flow to the structure.

3.1. CFD methods

In our CFD work, we used LES to simulate the airflow inside a realistic disk drive enclosure. A commercial code (CFD-ACE) using the algebraic dynamic sub-grid scale model (SGS) (Germano et al., 1991) was used. A single 3.5 in disk enclosed inside a fixed casing was used. The model used an e-block arm, suspensions, base plates and sliders.

Two cases were simulated:

(1) *Case* 1: A single e-block arm, suspension, base plate and slider was used. The slider was in contact with the disk on the bottom surface of the disk only.
(2) *Case* 2: Two e-block arms, suspensions, base plates and sliders were used. The disk was symmetrically actuated on both of its surfaces.

Relevant details of the model geometry are given in Table 1, information regarding the CFD modeling is given in Table 2, boundary conditions are described in Table 3 and finally, the information regarding the grid is give in Table 4. A top view of the grid is also shown in Fig. 1. Pressure data is transferred from the unstructured CFD grid to a structured grid (for calculating disk vibrations) by interpolation. Pressure values are linearly interpolated over one CFD cell to obtain the pressure at a node for the structural calculation. With respect to Fig. 1, we define a coordinate system whose origin is at the center of rotation of the disks. Azimuthal angles are then defined counter-clockwise with respect to a horizontal line through the origin. Two angular positions are of special importance: the angle where the shroud separates from its circular shape to accommodate the actuator (located at about 220°) and the angle where the shroud

Table 1
Geometry data

	Case 1	Case 2
Number of disks	1	1
Number of e-block arms	1	2
Number of base plates	1	2
Number of suspensions	1	2
Number of sliders	1	2
Disk thickness (mm)	1	1
Disk diameter (mm)	76.2	76.2
Width of shroud gap (mm)	1	1
Length of actuator (mm)	45	45
Length of e-block arm (mm)	32.5	32.5
Length of base plate (mm)	6.5	6.5
Length of suspension (mm)	11.1	11.1
Thickness of e-block arm (mm)	0.8	0.8
Thickness of base plate (mm)	0.3	0.3
Thickness of suspension (mm)	0.1	0.1
Dimensions of slider (mm)	$1 \times 0.8 \times 0.3$	$1 \times 0.8 \times 0.3$
Number of weight saving holes in e-block arm	2	2

Table 2
CFD modeling information

Governing equations	Filtered Navier Stokes equations
Solution algorithm	SIMPLEC (Van doormaal and Raithby, 1984)
Large eddy simulation model	Algebraic dynamic (Germano et al., 1991)
Type of LES filter	Top-hat (variable width)
Temporal differencing scheme	Crank Nicholson (second order)
Spatial differencing scheme (convective term)	Central differencing
Time step (s)	1.0×10^{-5}
Number of time steps	6000
Corresponding number of disk rotations	10
Initial conditions	Steady $k-\varepsilon$ solution

Table 3
Boundary conditions

Disks	Rigid rotating walls, no slip
Casing	Rigid wall, no slip
Hub/base of e-block arm	Fixed (similar to a cantilever)
Slider–disk interface	Slider slips on disk No cells between slider and disk
All structural interfaces (e.g. suspension + slider, e-block arm + base plate)	Rigidly joined (i.e. no dimple)
All fluid–structure surfaces	Walls, no slip

Table 4
Grid information

	Case 1	Case 2
Type of mesh	Structured grid mixed with quad-dominant unstructured cells	Structured grid mixed with quad-dominant unstructured cells
Number of cells	4 515 444	4 444 274
Average cell volume (mm^3)	5.7338×10^{-3}	5.7994×10^{-3}
Average grid resolution (mm)	0.1789	0.1796

reattaches itself closely to the disk periphery (located at about 340°). Fig. 1 also shows the refinement of the grid in the vicinity of the actuator arm. Finally three-dimensional outline views of the models are shown in Fig. 2. A schematic diagram showing cross-sectional dimensions of the simulation domain is shown in Fig. 3, for Case 2. The cross-section for Case 1 is identical, without an actuator above the disk.

Calculations were carried out on Linux-based clusters utilizing 64 CPUs. In spite of the massive computational power, our simulations needed to run for several weeks.

3.2. Structural modeling

A finite-difference code based on central differencing was developed to simulate the vibrating disk. The linearity of Eq. (1) and the periodicity of the azimuthal coordinate makes it a prime candidate for a hybrid-spectral method. Firstly, the primary variable w (transverse disk vibration) is Fourier transformed in the periodic direction (ϕ) resulting in a PDE of independent variables r and t:

$$w(r,\phi,t) = \sum_{m=-N/2+1}^{N/2} \hat{w}(m,r,t)\mathrm{e}^{\mathrm{i}m\phi}; \quad \frac{\partial}{\partial\phi} \to \mathrm{i}m. \tag{10}$$

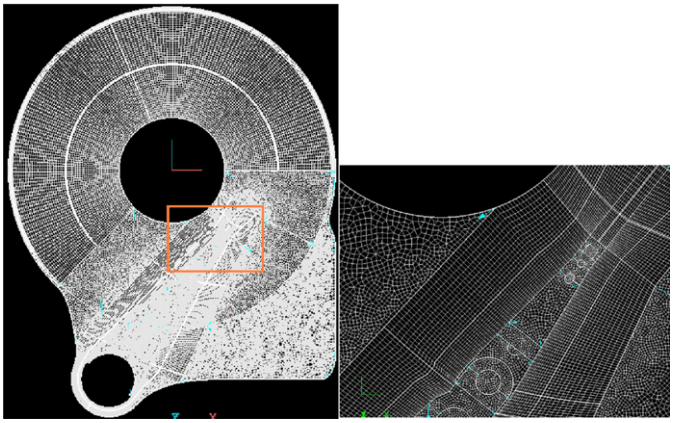

Fig. 1. Top view of the computational grid shown to the left. Highlighted region is zoomed in on the right to show the refinement near the actuator arm.

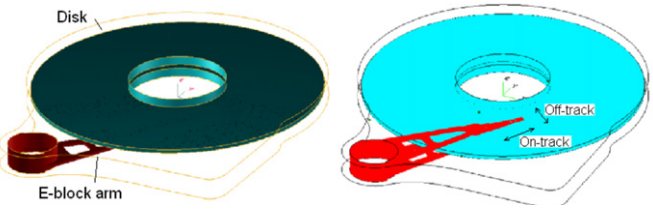

Fig. 2. Three-dimensional simplified view of the simulated Case 1 (left) and Case 2 (right).

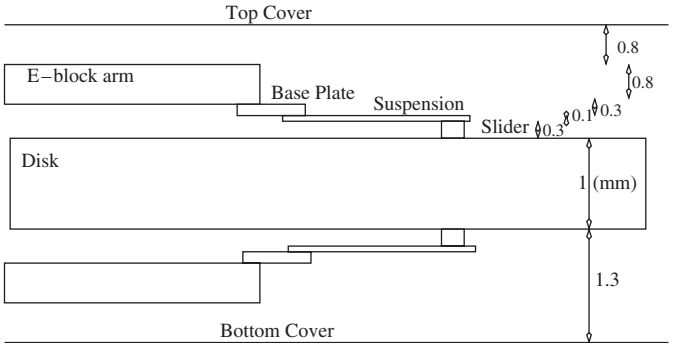

Fig. 3. Schematic diagram showing cross section of simulation domain for Case 2. Cross-section for Case 1 is identical, without an actuator above the disk.

Transforming Eq. (1), the following equation is obtained:

$$\rho h(\hat{w}_{,tt} + 2im\Omega\hat{w}_{,t} - m^2\Omega^2\hat{w}) + \frac{Eh^3}{12(1-\nu^2)}\hat{\nabla}^4\hat{w} - \frac{h}{r}\left(\sigma_{rr}r\hat{w}_{,r}\right)_{,r} + \frac{m^2h\sigma_{\phi\phi}}{r^2}\hat{w} = \Delta\hat{p} + \frac{1}{r}\delta(r-\xi)\delta(\phi)\hat{f}_z, \tag{11}$$

where

$$\hat{\nabla}^4 = \left(\frac{\partial^2}{\partial r^2} + \frac{1}{r}\frac{\partial}{\partial r} - \frac{m^2}{r^2}\right)^2 \tag{12}$$

and $\Delta\hat{p}$ and $\hat{f}_z$ are the corresponding transformed pressure differential and slider force on the disk.

Central differencing is used for the radial direction. The Laplacian operator $\nabla^2 w$ is treated specially due to the polar coordinate system:

$$\nabla^2 w = \left(\frac{\partial^2}{\partial r^2} + \frac{1}{r}\frac{\partial}{\partial r} - \frac{m^2}{r^2}\right) w = \left(\frac{1}{r}\frac{\partial}{\partial r}\left(r\frac{\partial w}{\partial r}\right) - \frac{m^2 w}{r^2}\right)$$
$$\Rightarrow \nabla^2 w_i \approx \frac{1}{r_i}\frac{1}{\Delta r^2}(r_{i+1/2}(w_{i+1} - w_i) - r_{i-1/2}(w_i - w_{i-1})) - \frac{m^2 w_i}{r_i^2}. \quad (13)$$

This method is second-order consistent and is easy to implement in an implicit time integration method. The biharmonic operator is discretized by the recursive application of the above stencil. The other terms of Eq. (1) are discretized using standard central differences. Due to the spectral representation of one dimension of the primary variable derivatives in ϕ are exact and are computed much faster than conventional finite differences. Moreover, due to the linearity of the equations, the different Fourier modes may be integrated independently of each other, and forward and backward transforms need only be taken for initializing or post-processing the calculation.

3.2.1. Treatment of boundary conditions

The boundary conditions of Eqs. (8) and (9) are also discretized using central differencing in the same manner as the governing equation. The governing equation (Eq. (1)) is discretized and solved on all radial points in the domain. Since the central-difference stencil consists of five points (two on each side of the central node) the numerical method requires the solution value at two additional points beyond the inner and outer boundaries of the disk. The addition of these "ghost points" is helpful in maintaining second-order consistency of our method (Thomas, 1998). Finally, the solution values at the ghost points are expressed in terms of solutions in the actual domain by using the discretized boundary conditions.

3.2.2. Time integration

The well-known first-order Newmark's algorithm is used for integrating Eq. (1) in time. Since the method is implicit, a linear system needs to be inverted at every time step. However, since the Fourier modes are decoupled, a single global matrix may be constructed for each mode and inverted only at the start of the calculation. Thereafter, the calculation is progressed by the application of these stored inverted matrices. The principal advantage of using Newmark's method over other conventional ODE integrators is the controllable numerical dissipation. Plots of the spectral radii of various Newmark's methods are widely available (Fung, 2003) and the two Newmark parameters (commonly referred to as β and γ) may be used to dissipate spurious high frequency oscillations in the solutions. Since the dissipation introduced is only numerical, the frequencies of the modes do not shift, as they would when using a model for the material damping. Unless explicitly noted all of our simulations used the standard values of $\beta = 0.5$ and $\gamma = 0.25$ which are nondissipative.

4. Validation of the code

Validation of codes is considered as an essential element of the code development process. Before we used our code to produce and report results, the code is put through a series of numerical tests and benchmarked against some well-known data. First some numerical tests of convergence are presented and then the code was validated against published results. The comprehensive test results presented here should help readers in assessing the simulation numerical uncertainty of our work.

4.1. Tests of convergence

By a Taylor series expansion it is easy to see that our discretization scheme is second-order consistent in the radial direction. In addition the stability properties of the first-order Newmark algorithm are also well known (unconditionally stable for $\beta \geqslant \frac{1}{2}$ and $\gamma \geqslant \frac{1}{4}(\frac{1}{2} + \beta)^2$) and carry over directly to our numerical scheme. For this reason we directly prove the convergence of our code based on numerical experimentation.

Firstly, while keeping the time step constant, the radial mesh size is varied. The $\mathscr{L}_2$ norm of the absolute error (denoted by ε, based on the finest radial resolution (1.95×10^{-3})) is then computed and plotted as a function of the radial mesh size, as shown in Fig. 4. The slope of the curve approximated by a linear curve fit is 1.87 which is close to the theoretical value of 2.0. This confirms that our central differencing scheme is convergent to second order in the radial direction.

Next, while keeping the radial mesh size constant, the time step is varied. While reducing the size of the time step (Δt) computations are carried out for correspondingly longer durations and solution values are recorded at 10 well-defined

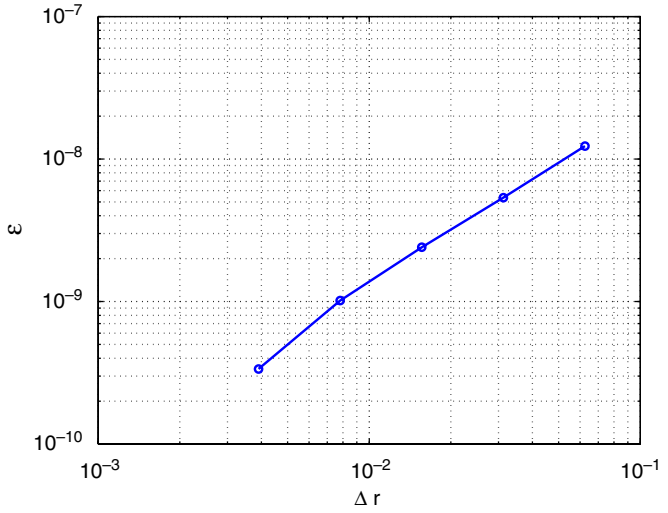

Fig. 4. Radial convergence: $\mathscr{L}_2$ norm of the error (ε) as a function of the radial mesh size (Δr).

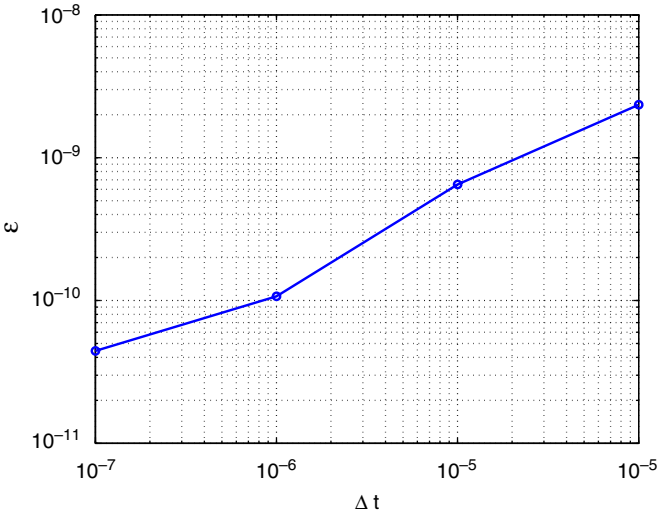

Fig. 5. Temporal convergence: $\mathscr{L}_2$ norm of the error (ε) as a function of the time step (Δt).

points in time. The $\mathscr{L}_2$ norm of the absolute error (again, denoted by ε) is plotted as a function of (Δt) in Fig. 5. While the data points do not fit a linear curve perfectly, the best curve fit to the data indicates an order of 0.7, which is close to the theoretical order of 1.0. Again this proves that our implementation of the Newmark's algorithm is first-order convergent.

4.2. Modal analysis

As a test of validation for our code, we compare the modal frequencies obtained from our finite-difference code with previously published theoretical and experimental data, and also results from the commercial code ANSYS.

In the thesis of D'Angelo (1991) a steel disk of outer diameter (OD) 356 mm, inner diameter (ID) 106.7 mm and thickness 0.775 mm was used to make measurements. Table 5 compares the natural frequencies of the modes of this

Table 5
Comparison of natural frequencies of a stationary disk

Mode	Current work (Hz)	Experiments		Theory		ANSYS	
		(Hz)	% Diff	(Hz)	% Diff	(Hz)	% Diff
(0,1)	36	37.19	3.20	39.08	7.88	38.06	5.41
(0,0)	40	38.40	−4.17	39.73	−0.68	38.68	−3.42
(0,2)	46	47.10	2.34	47.46	3.08	46.20	0.44
(0,3)	77	79.78	3.48	79.18	2.75	77.10	0.13
(0,4)	124	133.08	6.82	131.64	5.80	128.30	3.35
(0,5)	189	202.18	6.52	200.16	5.58	195.27	3.21
(1,0)	236	250.18	5.67	254.18	7.15	247.31	4.57
(1,1)	246	262.38	6.24	266.23	7.60	259.00	5.02
(0,6)	269	285.71	5.85	282.68	4.84	276.19	2.60
(1,2)	280	304.79	8.13	303.88	7.86	295.50	5.25
(1,3)	348	374.92	7.18	370.12	5.98	359.53	3.21

Note: Experimental and theoretical data is from D'Angelo (1991).

stationary disk computed using our finite-difference code with the theoretical and experimental prediction of D'Angelo (1991). The modes are described by a pair of integers (d, c) such that d is the number of nodal diameters and c is the number of nodal circles. In our simulations the impulse response of the disk was used to extract the modal frequencies. The theoretical calculations used a spectral Galerkin method while the experimental setup used a inductance-based Tektronic Modal Analyzer. Also included in Table 5 are the results obtained from the commercial code ANSYS. The results essentially show that our code can predict the natural frequencies of a stationary disk to reasonable accuracy. Generally, the discrepancies between our frequencies and the others increase with the mode number. The maximum difference between our results and the results across all columns is about 8%.

4.3. Variation of natural frequencies with rpm

As a final test we demonstrate the ability of the code to predict the dynamics of disks under rotation. The modal analysis presented in Section 4.2 is for a stationary disk. It is well known that the (nonaxisymmetric) disk modes split up into forward and backward traveling waves under rotation. Theoretically, in the absence of damping, the frequencies increase for forward traveling waves and decrease for backward traveling waves with a slope equal to $d\Omega$, where d refers to the number of nodal diameters of the mode. The speed of rotation at which the backward wave becomes a stationary wave is called the critical speed. Beyond the critical rpm, frequencies increase again and the wave is called the reflected wave.

Figs. 6 and 7 show the effect of rotation on several modes of the disk. Damping (especially of the surrounding air) has been omitted in this calculation. Since the frequencies of the modes are fairly close to each other, it is convenient to study the behavior of the modes separately. Generally, for a given number of nodal diameters, changing the number of nodal circles changes the frequency considerably, hence modes with the same number of nodal diameters but different circles are visualized on the same figure. The frequencies presented here are for a 3.5 in disk that was used in our CFD simulations. The modes of the stationary disk computed using ANSYS are given in Table 6 and they compare well with the results presented in this section. Table 6 also gives the theoretical frequencies of the modes at 10 000 rpm.

As expected, Fig. 6 shows that the axisymmetric modes $(0, 0)$ and $(0, 1)$ do not form forward (F) and backward (B) waves. Fig. 6 also shows the formation of $(0, 1)_{F,B}$ and $(1, 1)_{F,B}$ and Fig. 7 shows the formation of $(0, 2)_{F,B}$ and $(1, 2)_{F,B}$. Interestingly mode $(0, 2)_B$ goes critical at about 20 000 rpm which is shown more clearly to the right of Fig. 7.

5. Discussion on CFD results

5.1. Characterization of pressure loading

5.1.1. Mean and RMS values of the pressure loading

We begin by discussing the pressure loading on the disks. Figs. 8 and 9 (plotted to the same scale for comparison) show the *resultant* mean pressure on the disks (averaged over six revolutions of the computational period) for Cases 1 and 2, respectively. The resultant pressure is calculated as the sum of the pressure at the top and bottom surfaces of the

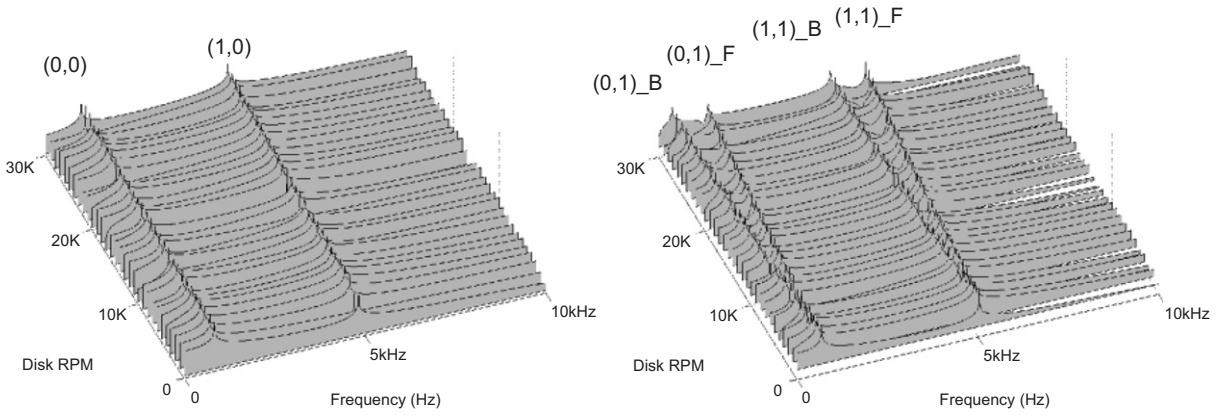

Fig. 6. Waterfall plot showing the natural frequencies as a function of rpm. Axisymmetric modes $(0,0)$ and $(1,0)$ to the left and modes $(0,1)$ and $(1,1)$ which split into forward and backward traveling waves to the right.

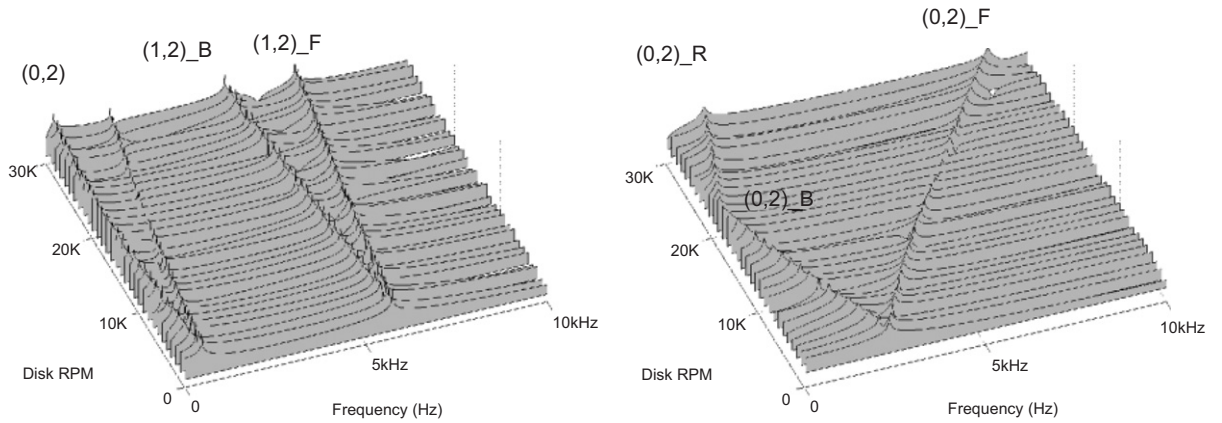

Fig. 7. Waterfall plot showing the natural frequencies of modes $(0,2)$ and $(1,2)$ as a function of rpm. Zoomed in view to the right shows the critical speed of the mode $(0,2)_B$ and the formation of the reflected wave $(0,2)_R$.

disk—with positive pressures acting vertically out of the plane of the paper. Plots depicting the pressure may be nondimensionalized by $\frac{1}{2}\rho U_{\text{disk}}^2(r)$, but we refrain from doing this since it would be misleading to compare such pressure coefficients directly. The mean pressure is close to zero for Case 2 (hence the fully dark region in Fig. 9) in almost all parts of the disk because of the inherent (axial) symmetrical nature of the flow domain. There do exist slight nonzero pressures at the edge of the disk (especially in the wake) which are numerical artifacts occurring because the statistics have not converged in that region.

The pressure distribution of Case 1 in Fig. 8 shows some interesting features. Firstly, the resultant pressure is higher at the inner hub and lower at the outer hub. In Case 1 the lack of obstruction in the upper portion of the drive creates a strong radial pressure gradient. However, in the lower part of the model, the actuator blocks part of the flow which equalizes the radial pressure gradient and increases the pressure upstream of the arm, especially nearer to the hub. The resulting asymmetry causes higher resultant pressure at the hub. Closer to the outer periphery the shroud acts as a mechanism to equalize the pressure between the top and bottom parts of the drive, hence the resultant pressure load is smaller at the outer edges of the disk. The obstructing actuator creates a stagnating flow upstream which leads to higher upstream pressures. This feature is also clearly manifested in Fig. 8.

Figs. 10 and 11 show the root mean square (r.m.s.) of the resultant pressure variation on the disk surface. Everywhere in this paper, the r.m.s. is calculated and reported about the mean. The r.m.s. values are much higher at the edge of the disk (especially from the shroud separation to its reattachment), but the plots have a truncated gray-scale to accommodate most of the flow domain. Figs. 10 and 11 show some similar features: (i) large r.m.s. pressure fluctuations

Table 6
Natural frequencies and modes of the disk, obtained from ANSYS

Mode no.	Frequency (Hz)	Mode (d,c)	Forward mode at 10 K rpm	Backward mode at 10 K rpm
1	781.56	(1,0)	948.23	614.89
2	802.71	(0,0)	–	–
3	946.65	(2,0)	1279.98	613.32
4	1610.9	(3,0)	2110.90	1110.90
5	2704.4	(4,0)	3371.07	2037.73
6	4126	(5,0)	4959.33	3292.67
7	5104.3	(0,1)	–	–
8	5355.1	(1,1)	5521.77	5188.43
9	5837.6	(6,0)	6837.60	4837.60
10	6147.3	(2,1)	6480.63	5813.97
11	7552.3	(3,1)	8052.30	7052.30
12	7826.9	(7,0)	8993.57	6660.23
13	9588.1	(4,1)	10 254.77	8921.43
14	10 090	(8,0)	11 423.33	8756.67
15	12 194	(5,1)	13 027.33	11 360.67
16	12 624	(9,0)	14 124.00	11 124.00
17	14 773	(0,2)	–	–
18	15 071	(1,2)	15 237.67	14 904.33
19	15 271	(6,1)	16 271.00	14 271.00
20	15 430	(10,0)	17 096.67	13 763.33
21	15 991	(2,2)	16 324.33	15 657.67
22	17 599	(3,2)	18 099.00	17 099.00
23	18 507	(11,0)	20 340.33	16 673.67
24	18 736	(7,1)	19 902.67	17 569.33
25	19 951	(4,2)	20 617.67	19 284.33
26	21 855	(12,0)	23 855.00	19 855.00
27	22 541	(8,1)	23 874.33	21 207.67
28	23 065	(5,2)	23 898.33	22 231.67
29	25 475	(13,0)	27 641.67	23 308.33
30	26 659	(9,1)	28 159.00	25 159.00

at the periphery and smaller fluctuations at the inner hub; (ii) a sharp increase in fluctuations at the shroud expansion; (iii) larger fluctuations in the wake formed behind the arm(s); and (iv) gradual reduction in the fluctuations downstream of the arm. Overall, the r.m.s. for Case 2 is more than for Case 1—which is a result of the turbulent flows on both sides of the disk. Finally, we also note that the presence of the arm causes a sharp break in axisymmetry, both in the mean and r.m.s. The loading process is thus nonuniformly distributed across several spatial scales and time scales as characteristic of turbulent flows. Hence most analytical models cannot provide an accurate description of the loading.

5.1.2. Frequency contribution to the r.m.s.

In addition to understanding the mean and r.m.s. of the pressure loading, it is important to understand its spectral content. It is well known that turbulent flows in hard drives are composed of a broad range of forcing frequencies, distributed typically from 0 to 10 kHz (the distribution is strongly a function of the Reynolds number).

The r.m.s. fluctuations of the pressure broken up into contributions from various frequency bands are shown in Fig. 12 for Case 1 and Fig. 13 for Case 2. In each figure, the r.m.s. pressure fluctuations are plotted as a function of the radius, from the ID to the OD. MD corresponds to the "middle diameter" of the disk. The r.m.s. contribution across different frequency bands may be easily computed using the Parseval's theorem.

Fig. 12(a) shows the fluctuations in the near wake region (326° from the origin). In this position, we notice the high fluctuations in the outer portion of the disk which is being impacted by the eddies shed from the arm. These fluctuations are comparable to the mean value of the pressure itself. The majority contribution to the fluctuations is from the low frequency components, 0–1 and 1–2 kHz. Towards the ID, fluctuations are much smaller, and are almost solely

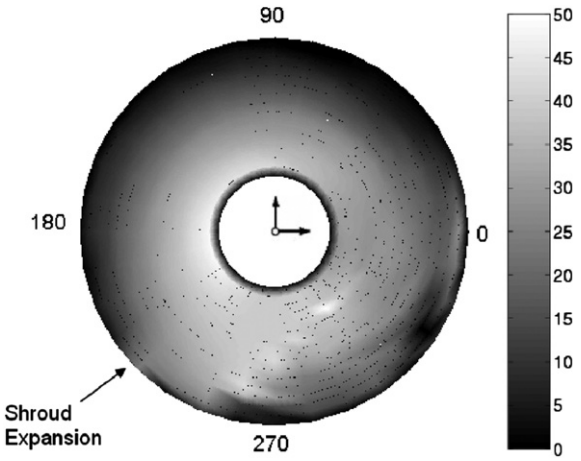

Fig. 8. Mean resultant pressure distribution on the disk for Case 1.

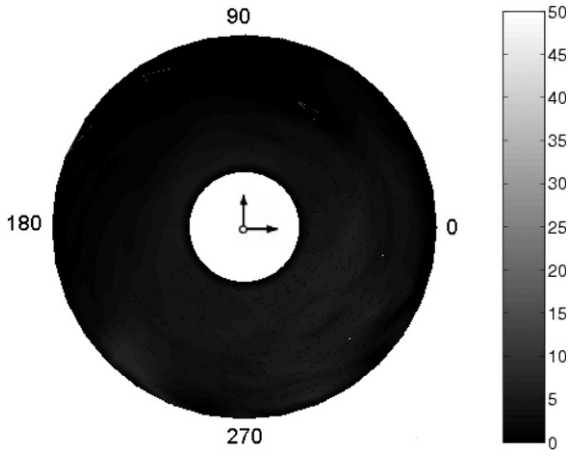

Fig. 9. Mean resultant pressure distribution on the disk for Case 2.

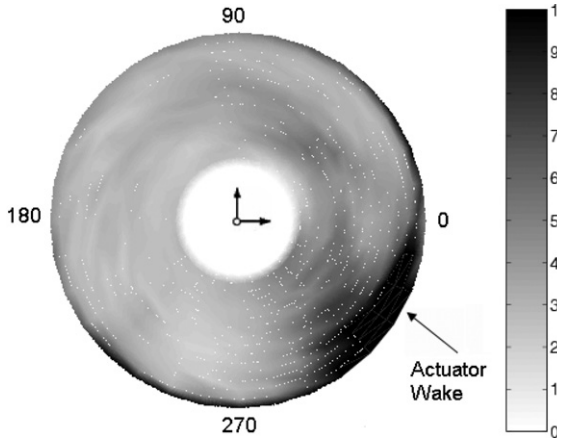

Fig. 10. The r.m.s. resultant pressure distribution on the disk for Case 1.

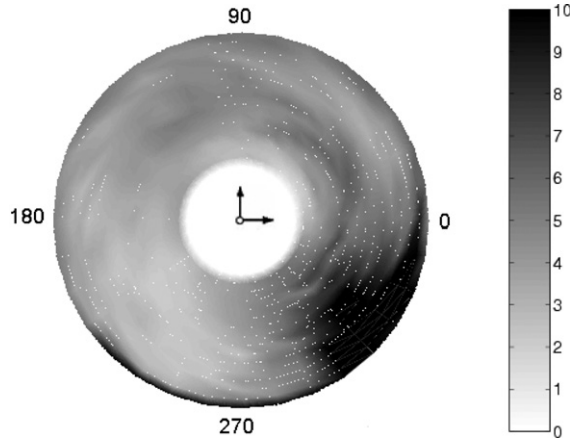

Fig. 11. The r.m.s. resultant pressure distribution on the disk for Case 2.

composed of the low frequency 0–1 kHz forcing. The peak in r.m.s. is not located at the edge of the disk but at one position before the OD. As the flow progresses azimuthally, the fluctuations on the disk damp out quickly. The r.m.s. fluctuations at 0° (shown in Fig. 12(b)) are about half of what they were 34° upstream. This rapid reduction of fluctuations appears across all frequency bands. As the flow progresses through the rest of the drive, the overall fluctuations reduce through the effects of viscous and SGS dissipation. The effects of the wake appear to move from the OD to the MD in Fig. 12(c) and (d) and the fluctuations are almost completely dissipated by 180° in Fig. 12(e). A common observation in Fig. 12(a)–(e) is the relatively higher r.m.s. at the edge of the disk. The higher r.m.s. values are due to the turbulent flow in the shroud gap and the resulting force has r.m.s. contributions from higher frequencies, up to 10 kHz. Finally, an interesting consequence of the shroud expansion is shown in Fig. 12(f) at 236° from the origin. The figure shows very high fluctuations at the outer edge of the disk with significant contributions from 0–1, 1–2 and 2–6 kHz frequencies. Apparently, the shroud expansion causes massive flow separation and generation of turbulence, with intensities that are comparable with those in the wake of the arm.

For completeness, Fig. 13 shows the r.m.s. pressure plots for Case 2, for the same angular positions as in Case 1. The figure shows that Case 2 has slightly higher fluctuations compared to Case 1, due to the turbulence generated on both sides of the disk. The figure for Case 2 demonstrates much of the same qualities as discussed above for Case 1: high r.m.s. fluctuations in the wake, high frequency contributions to fluctuations due to the flow in the shroud gap and very high r.m.s. due to the shroud expansion.

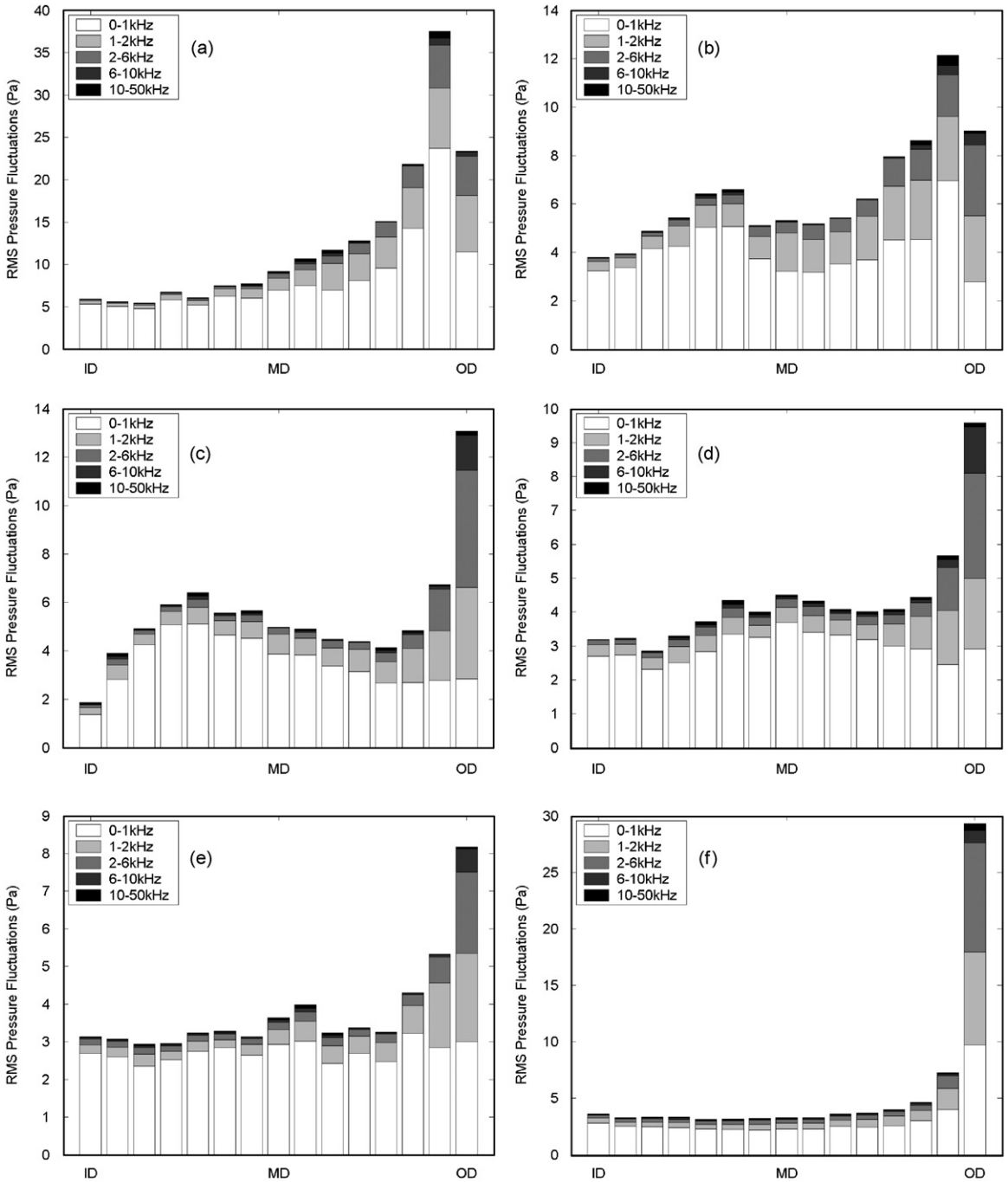

Fig. 12. The r.m.s. pressure fluctuations, broken down into contributions from different frequency ranges for Case 1. (a) 326°, (b) 0°, (c) 56°, (d) 112°, (e) 180°, and (f) 236°.

5.2. Axial flow in the shroud

The r.m.s. of the axial flow in the shroud gap (i.e. the component of the flow perpendicular to the plane of the disks) is shown in Fig. 14 for the complete azimuthal span (0–360), for three different axial positions: $z = 3.3$ corresponds to the top surface of the disk, $z = 2.8$ corresponds to the mid-plane of the disk and $z = 2.3$ corresponds to the bottom surface

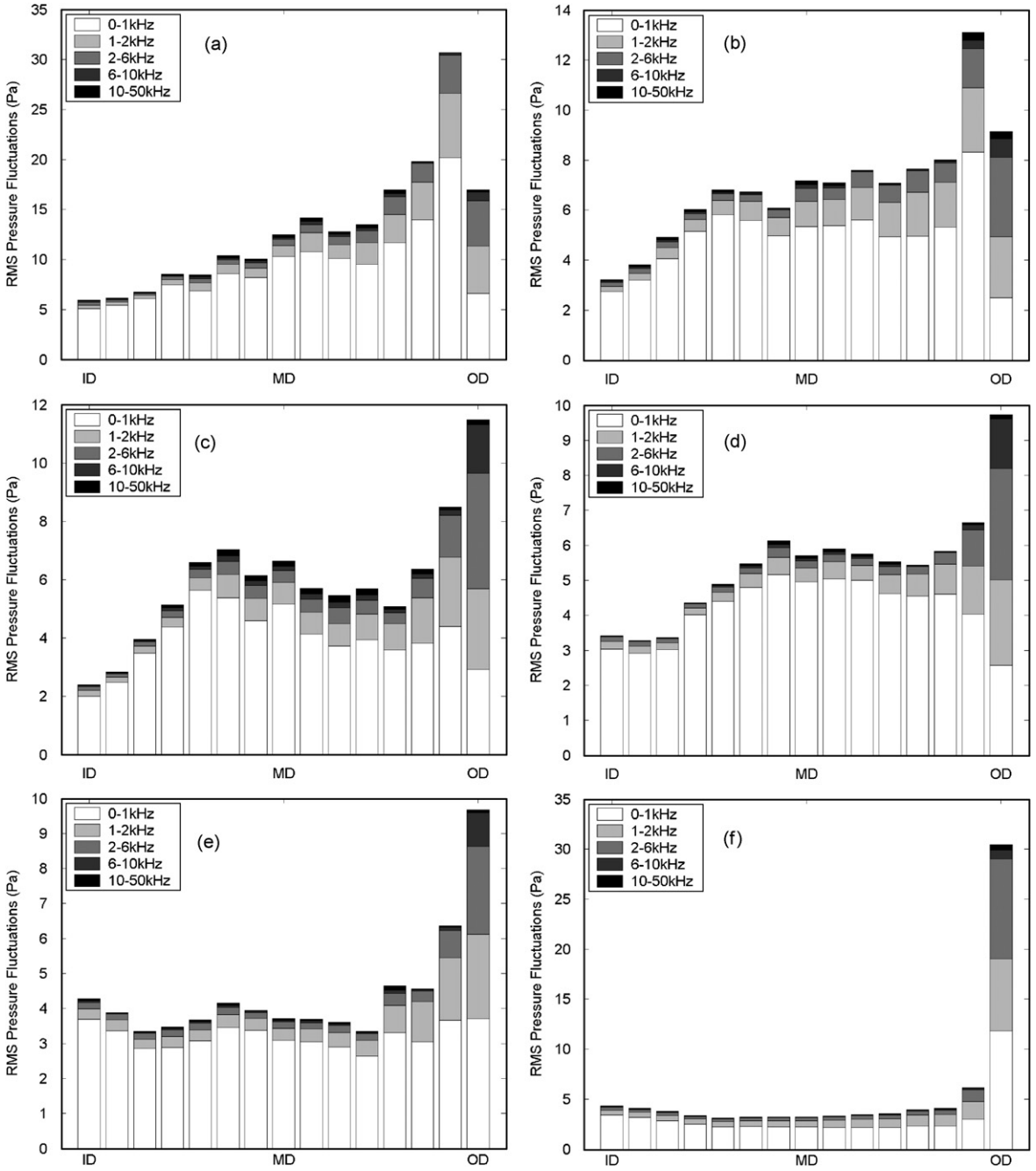

Fig. 13. The r.m.s. pressure fluctuations, broken down into contributions from different frequency ranges for Case 2. (a) 326°, (b) 0°, (c) 56°, (d) 112°, (e) 180°, and (f) 236°.

of the disk. The axial velocity is nondimensionalized, not by the mean axial velocity but by the disk edge velocity (Ωr_o), since the former is close to zero. The r.m.s. fluctuations of pressure at the same location as Fig. 14 are shown in Fig. 15. The strong correlation between the axial velocity fluctuations and the pressure fluctuations is clearly evident by comparing Figs. 14 and 15.

We notice that the fluctuations are fairly constant in the shrouded portion of the drive, with a very gradual decrease in the amplitude downstream of the wake. The r.m.s. of the fluctuations is a measure of the amplitude of the waves that

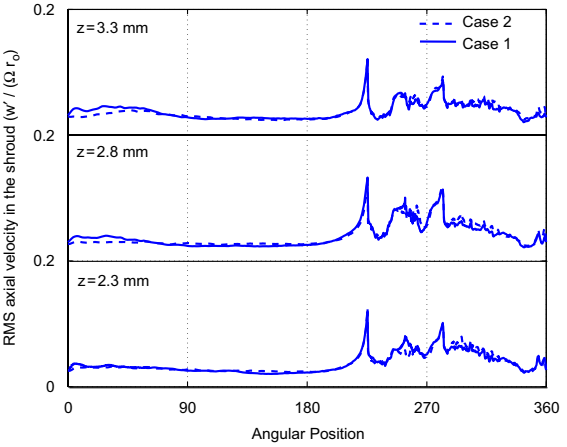

Fig. 14. The r.m.s. of the axial velocity at the center of the shroud gap, plotted for three different positions.

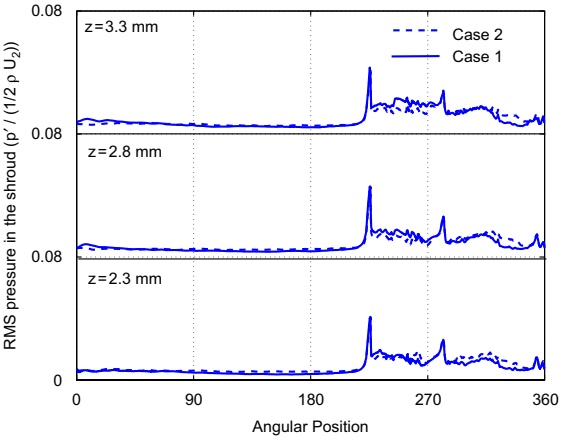

Fig. 15. The r.m.s. of the pressure fluctuations at the center of the shroud gap, plotted for three different positions.

the shroud gap can support. In both cases, the r.m.s. amplitude is small; close to 2% of the disk edge velocity. The presence or absence of an actuator simply does not matter, as there is very little difference between Cases 1 and 2. In agreement with our previous discussion, the shroud expansion causes very high fluctuations in the axial velocity (seen as the first large spike at about 220° in Fig. 14). The axial velocity fluctuates rapidly as the flow approaches and flows over the arm. The wake is characterized by a single peak immediately downstream of the arm, and several other peaks as the flow gets entrained back into the shrouded portion of the gap.

5.3. *Velocity profiles*

Much about the flow can be understood by studying the average velocity profiles between the disk and the stationary casing walls. Fig. 16 shows the time averaged nondimensional velocity profile $(\overline{u_\phi}(r)/\Omega r)$ as a function of the axial position between the disks for both Cases 1 and 2. The central solid band in the figure represents the disk. The profiles are shown, horizontally for different azimuthal positions (0−320°) and for three radial positions, ID (full line), MD (dashed line), and OD (dotted line). Each horizontal box spans the nondimensional magnitude from 0 to 1, while each vertical box spans the entire axial length of the domain, as shown: from the bottom cover to the top cover. Azimuthal positions are measured from the horizontal with respect to the disk centers, with the actuator being located at about 280° at MD.

In Fig. 16(a) which is for Case 1, one immediately observes the asymmetry of the velocity profiles. As expected, velocity profiles below the disk are smaller in magnitude than those above the disk, which is due to the loss in momentum by flowing over the arm. At about 240−280° we observe that the flow stagnates in the space below the disk—which is most likely due to the blocking effects of the actuator. Interestingly, the flow also stagnates in the space above the disk at the ID position (i.e. close to the hub). Since there is no arm present in this portion of the drive, the only reason for the formation of this recirculating flow would be the expanding section of the geometry. To clarify: once the flow has passed through the shrouded portion of the drive, it encounters an expanding section (to accommodate for the actuator). This expansion causes the flow to reverse direction close to the hub, where the linear velocity of the disk is the smallest. On the bottom side of the disk, the actuator blocks some of the expanded section, accelerating the flow slightly—which results in a higher velocity of the flow at 280−320°.

Velocity profiles for Case 2 in Fig. 16(b) are more symmetric than Case 1. Since the geometry, grid and boundary conditions are perfectly mirrored across the mid-plane, any lack of symmetry can only be attributed to insufficient data in the averaging process. In general, the velocity profiles look very similar to a turbulent Couette flow. There is a sharp fall off from the disk velocity in the boundary layer, a large core region of nearly constant velocity flow, followed by a sharp fall off to the stationary wall. It is also a general observation that the velocity profile is not completely flat in the central core region. Velocities are slightly higher in the region away from the disk. This can be mainly attributed to the axial location of the actuator. Referring to Fig. 3, the actuator is located closer to the disk than the fixed covers, hence the flow is decelerated in this region and accelerated closer to the covers. Fig. 16(b) also shows the following features of

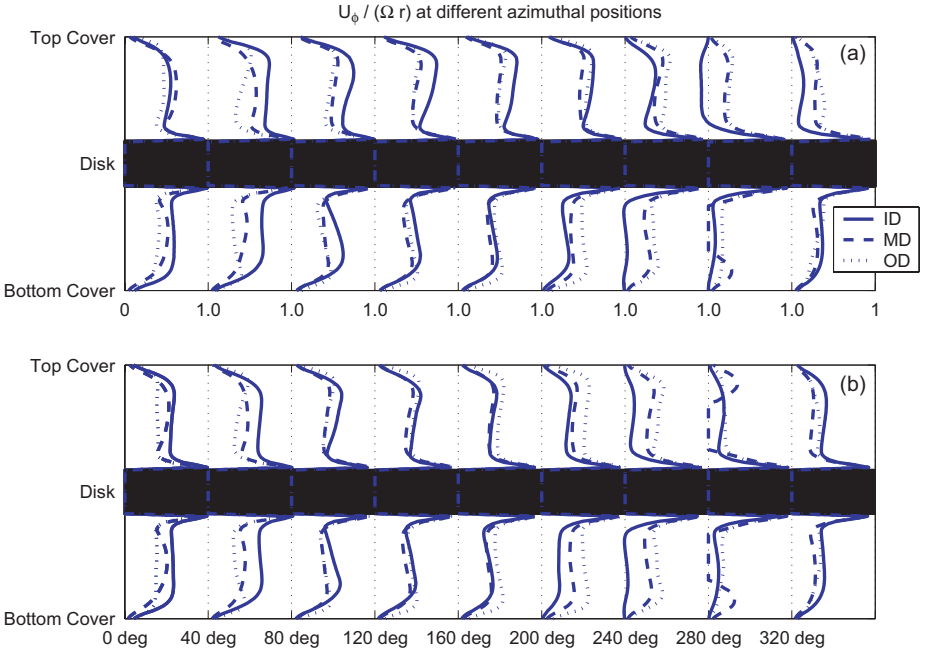

Fig. 16. Interdisk nondimensional velocity profiles for Case 1 (a) and Case 2 (b), shown as a function of the azimuthal angle, for three positions, ID, MD, and OD.

the flow: (i) the flow stagnates near the hub, upstream of the actuator arm; (ii) the velocity profile is small in the wake of the actuator and becomes fuller as it progresses azimuthally, gaining momentum from the rotating disks; (iii) from about 80° to about 200° the velocity profiles are very similar across ID-MD-OD positions; (iv) almost all velocity profiles have an inflection point near the disk.

5.4. Global quantities

The nondimensional kinetic energy (k^*) and windage (W^*, the rate of work done by the disks on the air in the computational domain) are plotted in Figs. 17 and 18 as a function of the number of disk rotations. These quantities determine the global energetics of the flow and help in understanding when the flow has achieved an energetic balance. Let U_o be the disk edge velocity, $\mathbb{V}$ be the volume of the computational domain, $\mathbb{A}$ be the area of the computational box, ν be the dynamic viscosity, $\overline{S_{ij}} = \frac{1}{2}((\partial\overline{U}_i/\partial x_j) + \partial\overline{U_j}/\partial x_i)$ be the filtered rate-of-strain tensor and τ_{ij}^R be the SGS (i.e. residual) stress tensor. The following quantities may then be defined as

$$U_o = \Omega r_o, \quad \mathbb{V} = \int_{\mathscr{V}} \mathrm{d}V, \quad \mathbb{A} = \int_{\partial\mathscr{V}} \mathrm{d}A,$$
$$k^* = \frac{\frac{1}{2}\int_{\mathscr{V}} \mathbf{u}\cdot\mathbf{u}\,\mathrm{d}V}{\frac{1}{2}U_o^2\mathbb{V}}, \quad W^* = \frac{\int_{\partial\mathscr{V}}(2\nu\overline{u_j}\overline{S_{ij}} - \overline{u_j}\tau_{ij}^R)\,\mathrm{d}A}{[\frac{1}{2}U_o^2][U_o]\mathbb{A}}. \tag{14, 15}$$

From Figs. 17 and 18 we notice that the kinetic energy in Case 2 is approximately 10% less than Case 1, which may be accounted for by the turbulent loss caused by the addition of an extra arm. However, the windage loss (i.e. the power required to drive the disks, or the rate of energy input to our computational domain) is about 2.5% smaller for Case 2 than for Case 1. This implies that with a slightly smaller rate of energy input, the Case 2 simulation saturates at a lower energy level, indicating the increased presence of dissipative processes such as vortex shedding and separation.

In reporting the kinetic energy and windage, the role of the initial conditions of the domain has been minimized by starting off both the simulations from a steady $k-\varepsilon$ solution. Moreover, the figures also show that the quantities achieve steady state in about four revolutions of the disk which gives confidence that the simulations have achieved statistical steadiness on a global level. For this reason, all statistics reported previously are only for the duration spanning 4–10 revolutions of the simulations.

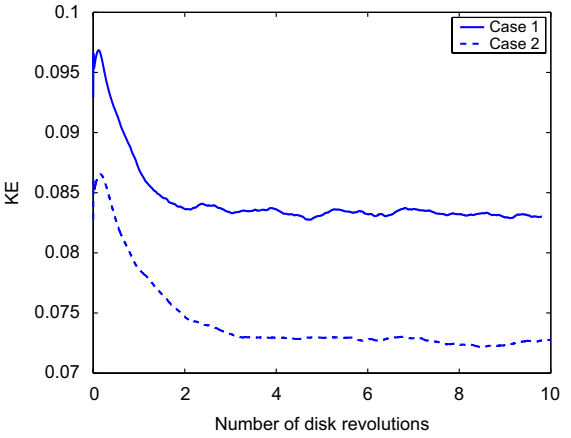

Fig. 17. Nondimensional kinetic energy (k^*).

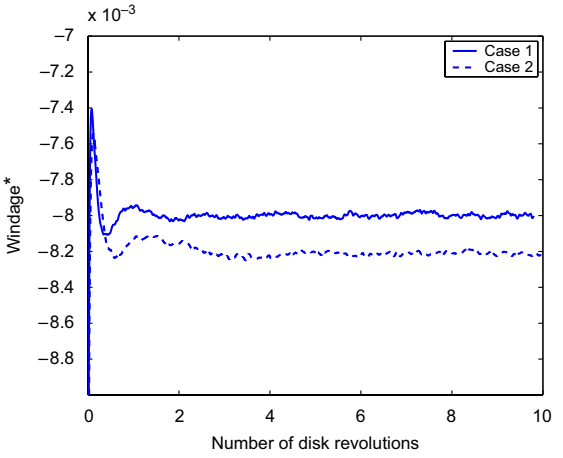

Fig. 18. Nondimensional windage (W^*).

While examining the forcing on the disk, it is useful to examine the forcing on the arm too. The coefficients of drag on the actuator arm are plotted as a function of time (with the first four revolutions removed) in Fig. 19 and the corresponding frequency spectra are plotted in Fig. 20. The drag and lift coefficients are decomposed into the off-track direction ($C_{D,\text{off}}$), the on-track direction ($C_{D,\text{on}}$) and the axial (out-of-plane) direction ($C_{D,z}$) using the projected areas of the actuator in those directions and the disk edge speed $U_o = \Omega r_o$. Fig. 21 summarizes the statistics of the data in Fig. 19. Interestingly, the figures show that the mean off-track drag coefficient, $\overline{C_{D,\text{off}}}$, is higher in Case 2 than in Case 1, but the trend is opposite for the on-track direction, $\overline{C_{D,\text{on}}}$. The additional e-block arm, suspension, base plate and slider in Case 2 increases the off-track projected area by only 25%, while the on-track projected area is the same. This indicates that the presence of the symmetric arms in Case 2 modifies the pressure field in the drive, such that the pressure gradient acting across the arm (in the off-track direction) is increased while the gradient in the direction of the arm (the on-track direction) is decreased.

6. Structural vibrations

Next the vibrations of the disk are calculated using the code previously discussed. The vibrations are initialized from rest and the pressure loading of the airflow and the slider are used as forcing functions on the right-hand side. An (r, m) grid of 32×64 was used and the resultant pressure recorded at each of the 2048 nodes was used in the calculation. The slider was modeled as a point load (delta function) superimposed on the airflow pressure distribution.

The vibrations of the disk are plotted as a function of time in Fig. 22 for both Cases 1 and 2. In plotting the displacements of the disk, since the vibrations under the slider are most important, various points were chosen from ID to OD passing through the location of the slider. The six subfigures shown in Fig. 22 are plotted for points located at 12.5%, 31.25%, 50% (MD), 62.5%, 81.25% and 100% (OD) of the radial span.

We notice that the vibrations have a positive bias (mean) for Case 1 which is expected given the positive mean pressure. The mean vibrations for Case 2 are close to zero. The vibrations of Case 2 clearly display a fundamental frequency (which from Table 6 is attributed to mode $(0,1)_B$). Case 1 does not clearly display this frequency and is apparently composed of higher frequency components. The other interesting observation is that the vibration results appear to be a linear function of the radius; i.e. the subfigures of Fig. 22 appear to be geometrically very similar except for the different scale used to plot them. This leads to the conclusion that most of the vibration energy is in the modes with zero nodal circles ($c = 0$). Given that the pressure fluctuations of the flow are mainly in the low frequencies (0–2 kHz) (recall Figs. 12 and 13), such a result is expected, since the first mode with one nodal circle ($c = 1$) is above 5 kHz and there are six modes of frequency lower than 5 kHz (with their corresponding forward and backward traveling frequencies; see Table 6).

A summary of the vibration results is presented in Fig. 23. It shows that the disk has a mean deflection for Case 1, due to the mean pressure bias. The r.m.s. vibrations about that mean are smaller than those for Case 2, but the resulting motions are larger for Case 1. The mean vibrations for Case 2 should theoretically be zero, but the small nonzero mean

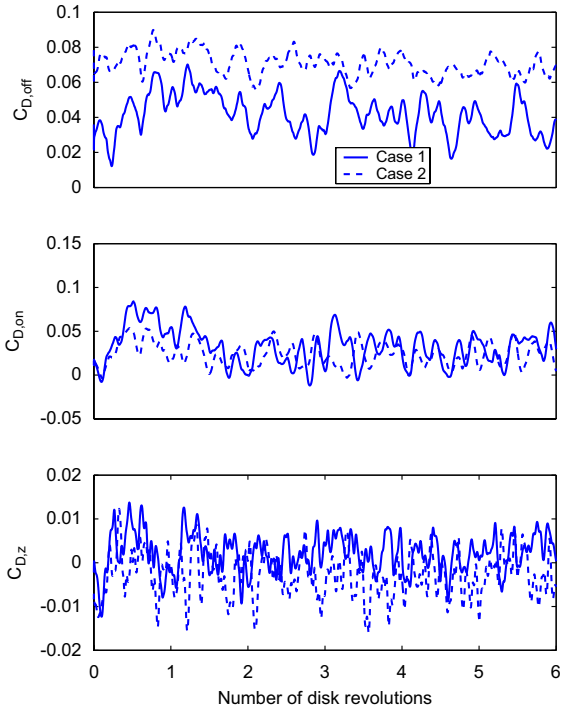

Fig. 19. Time history of variation of coefficients of drag on the actuator arm.

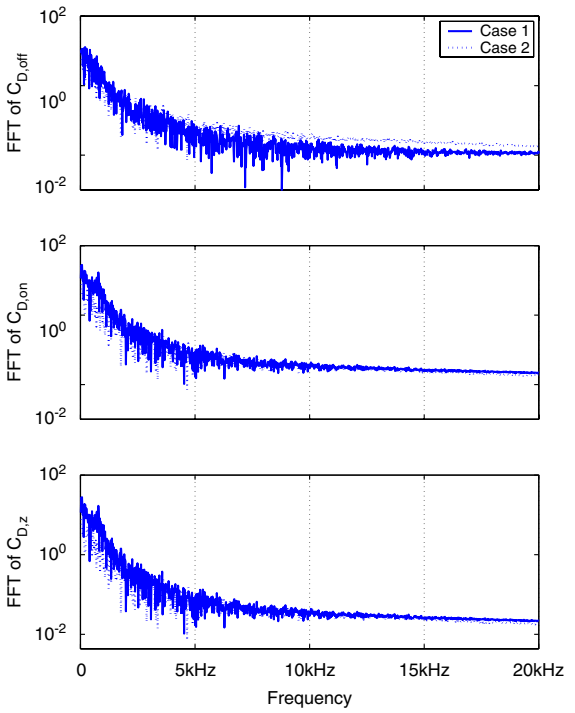

Fig. 20. FFT of drag coefficients on the actuator arm.

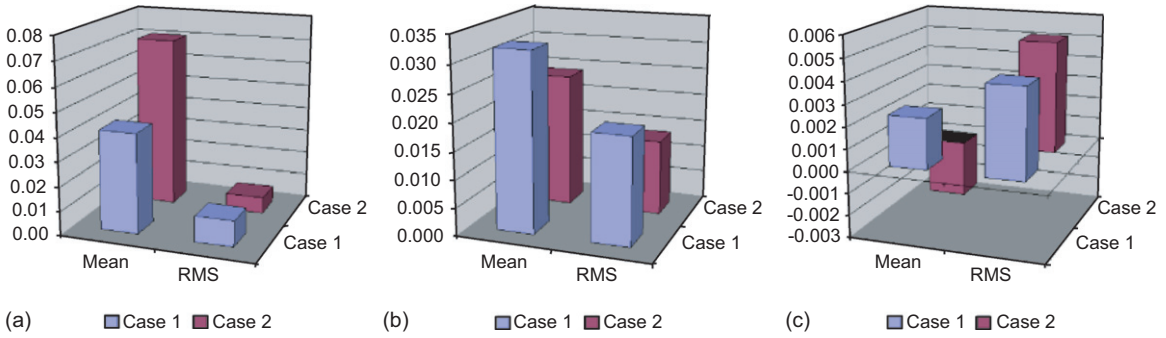

Fig. 21. Summary of statistics for coefficients of drag on the actuator arm: (a) $C_{D,off}$; (b) $C_{D,on}$; and (c) $C_{D,z}$.

is a result of partially unconverged statistics. The r.m.s. vibrations for Case 2 are large, approximately 680 nm. The results presented in Fig. 23 are in good agreement with experimental measurements of the disk vibrations, given in Imai (2001), Chang et al. (2002) and Guo and Chen (2001).

Due to the large number of modes in the 0–5 kHz range, the frequency spectra for the vibrations cannot be easily analyzed visually. It is more useful to understand the contributions to the r.m.s. from different frequency bands, as done earlier for the pressure fluctuations. As seen in Fig. 24, for Case 2, approximately 95% of vibration energy is in the 0–1 kHz range, which contains the top three modes. A small amount of energy is contained in the 1–5 kHz range, while there is virtually no contribution thereafter. This is the reason why the dominant frequency of Case 2 in Fig. 22 corresponds to the (0, 1) mode. For Case 1, approximately 20% of the energy is shifted from the 0–1 kHz range to the 1–5 kHz range. Given the mean deflection of the disk about its equilibrium, energy is transferred from the (0, 1) mode to higher modes (mode # 4–6) and this results in a smaller r.m.s. amplitude of vibration.

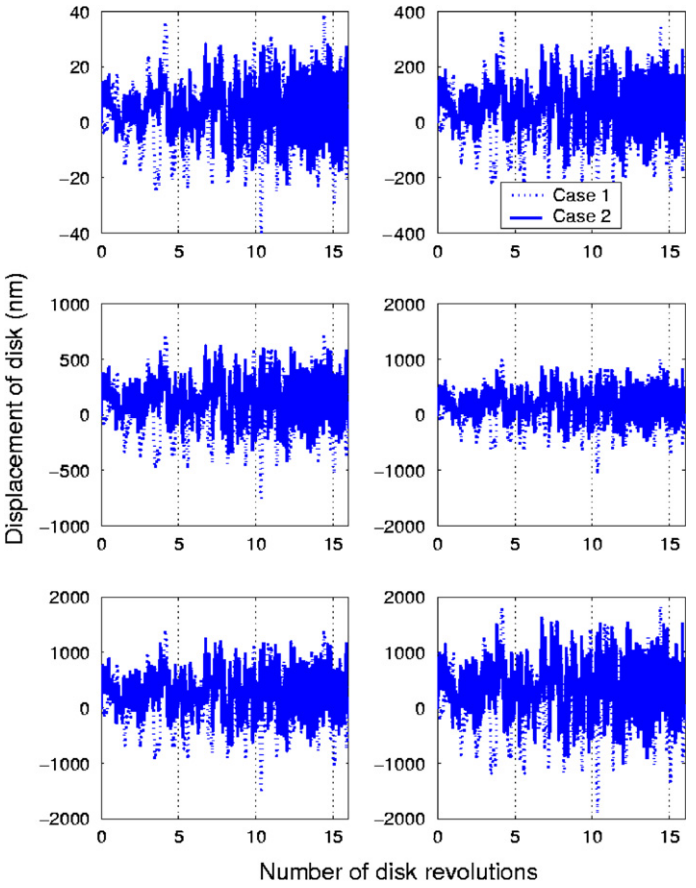

Fig. 22. Disk vibration results showing the displacement of the disk as a function of time. Results are shown for points located at 12.5%, 31.25%, 50% (MD), 62.5%, 81.25% and 100% (OD).

7. Conclusions and future work

The conclusions reached are summarized as follows.

(1) We have presented a methodology for computing the vibrations of the rotating disk in a hard disk drive, dealing with much more realistic airflow models than previous attempts. Given the complicated nature of the flow, calculations need to be repeated for even small changes to the drive configuration, (e.g. movement of the actuator from ID to OD), which makes a comprehensive investigation of all cases very expensive; almost impossible. However, we have provided two useful aids in the solution to such problems. (i) We have characterized the pressure loading in great detail for the two most commonly occurring cases (sliders flying on one or two sides of the disk) and (ii) we have described the numerical methods to accurately compute the flow and the structural solutions. Finally, we expect that the data presented will serve as a useful tool for benchmarking future calculations or experiments.

(2) In terms of the flow field, we found that the mean pressure loading for Case 1 is asymmetric, arising due to the asymmetry of the geometrical configuration. The r.m.s. vibrations of Case 2 are higher than those for Case 1 and their spectral distributions are almost identical. The spectra show that most of the energy is in the 0–1 kHz range and the r.m.s. increases with increasing radius. The wake and the shroud expansion show the highest fluctuations. While the formation of the wake behind the arm is inevitable, drive designers should avoid expanding diffuser-like cross-sections which act as a source of separation and generation of turbulence. We also found that the fluctuations in the shroud gap corellate very well with the pressure fluctuations—hence, it may be useful to measure the axial flow in the gap (say by PIV) when measurement of pressure is difficult. Finally, we also note that the velocity profiles between the disk and the casing resemble turbulent Couette flow very well, and may be used to model flows in other cases.

(3) In terms of the disk vibrations, we note that 1 mm thick, 3.5 in aluminum disks may be susceptible to critical behavior at about 20 000 rpm. Our results do not take into account changes in the flow field at those speeds and the

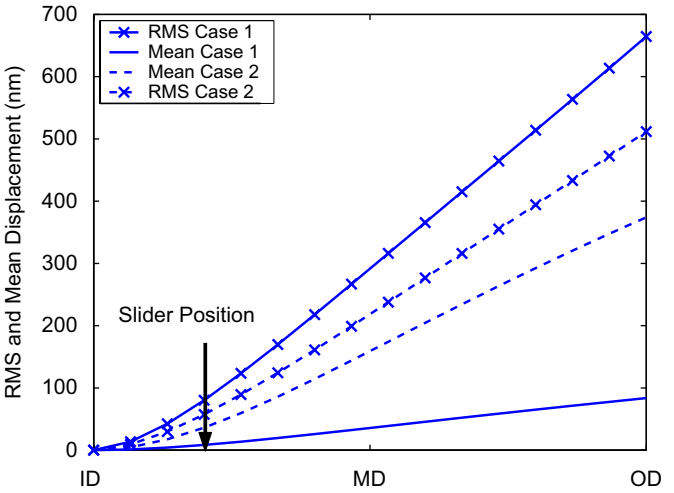

Fig. 23. Summary of disk displacement results.

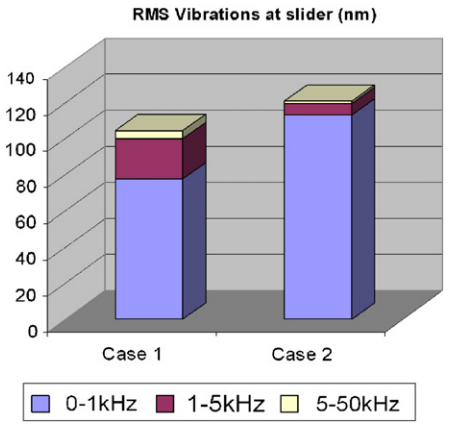

Fig. 24. Contribution to the r.m.s. disk vibrations under the slider from various frequency ranges.

resulting damping. Nonetheless, drives that operate in the 20 000–30 000 rpm range may be subject to these resonances. At 10 000 rpm our results show that for Case 1 the disk undergoes a mean asymmetric deflection and vibrates at a smaller magnitude in the higher modes. For Case 2, there is no mean deflection, and the disk primarily vibrates in the lowest fundamental mode.

(4) A direct continuation of this work would be to compute the resulting off-track and on-track motions of the slider-head, both due to the air drag and the disk motion. While this is currently unfeasible in our simulations, given the separation of scales, this could be the subject of another investigation that accounts for all the nonlinear dynamics of the slider motion.

Acknowledgments

This study was supported by the Computer Mechanics Laboratory (CML) at the University of California, Berkeley. The authors wish to acknowledge the contribution from Intel Corporation, Hewlett-Packard Corporation, IBM Corporation, and the National Science Foundation Grant EIA-0303575 in making hardware and software available for the CITRIS Cluster which was used in producing these research results.

References

Chang, Y.-B., Park, D.-K., Park, N.-C., Park, Y.-P., 2002. Prediction of track misregistration due to disk flutter in hard disk drive. IEEE Transactions on Magnetics 38 (2), 1441–1446.

Chung, J., Oh, J.-E., Yoo, H.H., 2000. Non-linear vibration of a flexible spinning disc with angular acceleration. Journal of Sound Vibration 231, 375–391.

D'Angelo, C., 1991. Vibration and aeroelastic stability of a disk rotating in a fluid. Ph.D. Thesis, University of California, Berkeley.

Fukaya, R., Obi, S., Masuda, S., Tokuyama, M., 2002. Flow instability and elastic vibration of shrouded corotating disk systems. Experiments in Fluids 33, 369–373.

Fung, T.C., 2003. Numerical dissipation in time-step integration algorithms for structural dynamic analysis. Progress in Structural Engineering and Materials 5 (3), 167–180.

GermGermano, M., Piomelli, U., Moin, P., Cabot, W.H., 1991. A dynamic sub-grid scale eddy viscosity model. Physics of Fluids A 3 (7), 1760–1765.

Guo, L., Chen, Y.-J.D., 2001. Disk flutter and its impact on hdd servo performance. IEEE Transactions on Magnetics 37 (2), 866–870.

Hosaka, H., Crandall, S., 1992. Self-excited vibrations of a flexible disk rotating on an air film above a flat surface. Acta Mechanica 3, 115–127.

Imai, S., 2001. Fluid dynamics mechanism of disk flutter by measuring the pressure between disks. IEEE Transactions on Magnetics 37 (2), 837–841.

Kang, N., Raman, A., 2004. Aeroelastic flutter mechanisms of a flexible disk rotating in an enclosed compressible fluid. Journal of Applied Mechanics (Transactions of the ASME) 71 (1), 120–130.

Kim, B.C., Raman, A., Mote, C.D., 2000. Prediction of aeroelastic flutter in a hard disk drive. Journal of Sound Vibration 238, 309–325.

Lamb, H., Southwell, R.V., 1921. The vibrations of a spinning disk. Royal Society of London Proceedings Series A 99, 272–280.

Tatewaki, M., Tsuda, N., Maruyama, T., 2001. A numerical simulation of unsteady airflow in hdds. FUJITSU Science and Technology Journal 37 (2), 227–235.

Thomas, J.W., 1998. Numerical Partial Differential Equations: Finite Difference Methods. Springer, New York.

Van doormaal, J.P., Raithby, G.D., 1984. Enhancements of the simple method incompressible fluid flows. Numerical Heat Transfer 7, 147–163.

Yuan, Z.X., Luo, A.C.J., Yan, X., 2004. Airflow pressure and shear forces on a rotating, deformed disk in an open shroud. Communications in Nonlinear Science and Numerical Simulation 9 (5), 481–497.